Soft Matter

RSC Publishing

PAPER

View Article Online
View Journal | View Issue

Cite this: *Soft Matter*, 2013, **9**, 3956

Different modulated structures of topological defects stabilized by adaptive targeting nanoparticles

George Cordoyiannis,*[abcd] Venkata Subba Rao Jampani,[b] Samo Kralj,[be] Surajit Dhara,[f] Vassilios Tzitzios,[g] Georgia Basina,[g] George Nounesis,[h] Zdravko Kutnjak,[bi] Chandra Shekhar Pati Tripathi,[a] Patricia Losada-Pérez,[a] Dalija Jesenek,[b] Christ Glorieux,[a] Igor Muševič,[b] Aleksander Zidanšek,[bei] Heinz Ameinitsch[j] and Jan Thoen[a]

Received 16th November 2012
Accepted 30th January 2013

DOI: 10.1039/c3sm27644a

www.rsc.org/softmatter

It is demonstrated that interactions between nanoparticles and topological defects induce a twist-grain boundary phase in a chiral liquid crystal. The occurrence of this phase, the analogue of the Shubnikov phase in type-II superconductors, is driven by direct interactions between surface-functionalized CdSe quantum dots and screw dislocations. It is shown that, within an adaptive-defect-core-targeting mechanism, nanoparticles of appropriate size and functionalization adapt to qualitatively different cores of topological defects such as disclination lines and screw dislocations. This mechanism enables the effective reduction of the energetically costly, singular defect core volume, while the surrounding phase ordering remains relatively weakly affected. The findings suggest new pathways towards the controlled assembly of superstructures in diverse, symmetry-broken, condensed-matter systems, ranging from nanoparticle-decorated liquid crystals to superconductors.

I Introduction

In the past few years there has been a rapidly increasing interest in the interactions of colloidal particles with topological defects in fluid matrices.[1–6] These added particles can induce chirality,[7] increase the dielectric anisotropy[8,9] and the electro-optical response of liquid crystals (LCs),[10] explore pathways towards tunable metamaterials,[4] enable self-healing mechanisms,[11] *etc.* The complexity of possible behaviors is large in the case of anisotropic liquids such as the LC phases. Inside the LC matrices the Goldstone excitation modes of a symmetry-breaking field introduce softness,[12] *i.e.*, a strong susceptibility to even weak local perturbations. The LC structures could be disrupted by the immersed particles,[1] giving rise to long-range forces and strong interactions with topological defects. The particles are attracted to locally elastically distorted LC regions and, thus, to topological defects.[3,13,14] The resulting elastic forces are exploited to trigger ordering or self-organization of particles into regular templates.[15–18]

Recently, a new family of nanoparticles (NPs) has been reported, capable of forming stable suspensions in LCs.[14] These NPs are spherical 3.5 nm diameter CdSe quantum dots, surface-treated with oleyl-amine (OA) and tri-octyl-phosphine (TOP). They significantly extend the stability range of blue phases (BPs) of chiral LCs. The stabilization effect was originally proposed by Kikuchi *et al.*[13] It is based on the reduction of the free energy penalty for forming defects *via* a partial replacement of their essentially isotropic core volume by captured polymers[13] or nanoparticles.[14]

In addition to BPs characterized by topological line defects in the orientational order, chiral LCs can also exhibit twist-grain boundary phases (TGBs) with topological line defects in the translational order. TGBs consist of a one-dimensional lattice of screw dislocations residing in planar grain boundaries that separate smectic blocks. They represent the LC analogue of the Shubnikov phase exhibiting Abrikosov flux-vortex configurations in type-II superconductors. Long after their prediction[19,20] and experimental discovery,[21,22] TGB_A (smectic-A blocks) and various types of TGB_C (smectic-C blocks) phases have been observed in pure compounds and mixtures of LCs and chiral dopants.[23,24] They exhibit particular thermal signatures,[25] X-ray patterns,[26] nuclear magnetic resonance spectra[27] and optical microscopy textures.[28]

[a]*Departement Natuurkunde en Sterrenkunde, KU Leuven, 3001 Leuven, Belgium. E-mail: george.cordoyiannis@ijs.si*

[b]*Condensed Matter Physics Department, Jožef Stefan Institute, 1000 Ljubljana, Slovenia*

[c]*Department of Physics, University of Athens, 15784 Athens, Greece*

[d]*EN FIST Center of Excellence, 1000 Ljubljana, Slovenia*

[e]*Department of Physics, University of Maribor, 2000 Maribor, Slovenia*

[f]*School of Physics, University of Hyderabad, Hyderabad 500046, Andhra Pradesh, India*

[g]*Institute of Materials Science, National Centre for Scientific Research "Demokritos", 15310 Aghia Paraskevi, Greece*

[h]*Biomolecular Physics Laboratory, National Centre for Scientific Research "Demokritos", 15310 Aghia Paraskevi, Greece*

[i]*Jožef Stefan International Postgraduate School, 1000 Ljubljana, Slovenia*

[j]*Institute of Inorganic Chemistry, Graz University of Technology, 8010 Graz, Austria*

In the present work we experimentally prove the existence of an adaptive-defect-core-targeting (ADCT) mechanism efficiently stabilizing even qualitatively different defect lattices in symmetry-breaking phases by using the same kind of NPs. It is demonstrated that CdSe quantum dots of appropriate size and surface functionalization exhibit the ADCT mechanism. In addition to BPs,[14] these NPs effectively stabilize TGBs.

The plan of the paper is as follows. The measured samples and experimental methods are described in Section II. In Section III we introduce a simple phenomenological model that is later used to interpret the measurements. The experimental results are presented in Section IV, followed by mean-field estimates focusing on NP-driven TGB_A stabilization in Section V. The results and basic principles of the ADCT mechanism are discussed in Section VI and summarized in Section VII.

II Materials and methods

Several mixtures of the chiral liquid crystal *S*-(+)-4-(2-methylbutyl) phenyl-4-decyloxybenzoate (CE6) with NPs have been investigated using high-resolution adiabatic scanning calorimetry, small-angle X-ray scattering and polarizing optical microscopy. CE6 exhibits all three BPs, and a cholesteric to smectic-A (N^*–SmA) transition at 314.5 K. The preparation of mixtures with different NP concentrations χ (defined as the mass of NPs over the total sample mass) has been described elsewhere.[29]

A High-resolution adiabatic scanning calorimetry (ASC)

The heat capacity (C_p) measurements were performed in a home-made, fully computerized adiabatic scanning calorimeter consisting of four stages (*i.e.*, sample and cell are surrounded by three shields). The air among them is being vacuum-pumped to achieve maximum insulation from the environment. The capability of adiabatic scanning calorimetry for the simultaneous and accurate determination of heat capacity and enthalpy enables high-resolution studies of phase transitions and critical phenomena.[30] The exceptional temperature stability of ± 50 μK and the slow scanning rates bring the sample close to the real thermal equilibrium, allowing the precise determination of phase diagrams. For the present experiments sample quantities of 1.7 g were placed in a 22 g tantalum cell. The heat capacity of the empty cell was measured in a separate control experiment and it was subtracted in order to derive the net C_p of the sample.

B Small-angle X-ray scattering (SAXS)

The X-ray measurements were performed in the Austrian Beamline,[31] located at ELETTRA Synchrotron (Trieste, Italy). An asymmetric-cut, double-crystal monochromator and a double-focusing toroidal mirror were used to produce a focused X-ray beam of 8 keV. The setup has a very high resolution, better than 0.001 $Å^{-1}$ (half-width at half-maximum). The samples are mounted in capillary tubes (Hingelberg Mark capillaries, no. 14) and the temperature is controlled by an in-house-built heating stage combined with a water bath (Huber Unistat). The temperature stability is in the order of ± 10 mK. No orientation has been imposed on the sample for X-ray measurements.

C Polarizing optical microscopy (POM)

For observation under the microscope, the samples were placed between 1 cm × 1 cm glass slides. For homeotropic cells, the glass surfaces were coated with octadecyl dimethyl (3-trimethoxysilylpropyl)ammonium chloride (ABCR GmbH), in order to obtain strong perpendicular surface-anchoring of the liquid-crystalline molecules on a chemisorbed DMOAP monolayer. For planar cells, a thin layer of polyimide (PI-2555, NISSAN Chemicals) was spin-coated on the surface of the glasses. A velvet cloth was used for unidirectional rubbing on polyimide for achieving a planar alignment on the glasses. A uniform cell thickness of 5 μm was obtained by using mylar spacers and the thickness was determined through transmission spectra using a fiber optic spectrometer (Ocean Optic, USB-2000). The cells were heated to 325 K, corresponding to the isotropic phase of CE6, and filled with the sample. The temperature was slowly changed by means of an Instec, STC 200 controller. The textures were observed under a polarizing optical microscope (Nikon, Eclipse E600 POL), using a color camera (PL-A742, Pixelink).

III Brief theoretical background

In order to qualitatively explain the observed key features, a rather simple phenomenological model can be used in terms of the nematic director field $\vec{n}$ and the smectic-A complex order parameter

$$\psi = \eta e^{i\phi}. \tag{1}$$

The unit vector $\vec{n}$ defines the local average uniaxial LC orientation, the translational order parameter η reveals the degree of smectic ordering and the phase factor ϕ determines the position of smectic layers.

In the free energy density expression $f = f_e^{(n)} + f_c^{(s)} + f_e^{(s)}$ we include only the essential terms that are needed for the results discussion. The nematic elastic free energy penalty is given by[12]

$$f_e^{(n)} = \frac{K_1}{2}\left(\nabla\cdot\vec{n}\right)^2 + \frac{K_2}{2}\left(\vec{n}\cdot\left(\nabla\times\vec{n}\right) - q_{ch}\right)^2 + \frac{K_3}{2}\left|\vec{n}\times\nabla\times\vec{n}\right|^2, \tag{2}$$

where K_1, K_2 and K_3 are the Frank nematic elastic constants, and q_{ch} stands for the chirality-enforced wave vector.

The smectic condensation and elastic free energy contributions are approximated by[12,32]

$$f_c^{(s)} = \alpha_0 t|\psi|^2 + \frac{\beta}{2}|\psi|^4, \tag{3}$$

$$f_e^{(s)} = C_{\|}|(\vec{n}\cdot\nabla - iq_0)\psi|^2 + C_{\perp}|(\vec{n}\times\nabla)\psi|^2. \tag{4}$$

The quantities α_0 and β are positive Landau expansion coefficients, and

$$t = \frac{T - T_*}{T_*} \tag{5}$$

is the reduced temperature. $C_{\|}$ and $C_{\perp}$ stand for the smectic compressibility and the bend elastic constant, respectively.

These constants are positive and enforce a SmA ordering with a layer thickness of $d = 2\pi/q_0$. Therefore, the smectic ordering minimizing the term $f_c^{(s)} + f_e^{(s)}$ below T_* could be expressed as $\psi_{eq} = \eta_s e^{iq0x}$, where it is assumed that the smectic layers are aligned along the x-axis and

$$\eta_s = \sqrt{\frac{-t\alpha_0}{\beta}} = \eta_0\sqrt{-t}. \quad (6)$$

The corresponding value of the smectic condensation term equals

$$f_c^{(s)} = -\frac{\alpha_0|t|\eta_s{}^2}{2} = -\frac{\alpha_0|t|^2\eta_0{}^2}{2}.$$

For the sake of simplicity it is henceforth assumed that $C = C_{\|} \sim C_{\perp}$. Apart from the smectic layer thickness and the chiral pitch length, there are additional important material-dependent lengths,[12] such as the smectic order parameter correlation length ξ and the nematic twist penetration length λ. Below T_* their values are roughly determined by

$$\xi = \sqrt{\frac{C}{\alpha_0|t|}} = \frac{\xi_0}{\sqrt{|t|}}, \quad (7)$$

$$\lambda = \sqrt{\frac{K_2}{q_0{}^2C\eta_s{}^2}} = \frac{\lambda_0}{\sqrt{|t|}}. \quad (8)$$

IV Experimental results

The phase transition behaviors of pure CE6 and three mixtures of CdSe NPs, $\chi = 0.0005$, 0.005 and 0.02, were measured using ASC. The temperature dependence of C_p, obtained upon slow cooling at an average rate of 1.6 mK min^{-1}, is shown in Fig. 1. CE6 exhibits a single, sharp, first-order anomaly corresponding to a direct N*–SmA transition, with a coexistence region of 52 ± 2 mK. Note that the presence of any TGB$_A$ order would be reflected in a significant broadening of the transition and changes in the C_p pre-transitional wings.[25] Such a characteristic feature was not found for pure CE6.

However, a dramatically different phase transition behavior is observed in the C_p data for CE6 + NP mixtures. A wider, double-peak anomaly has been observed for all NP concentrations, marking the presence of a thermodynamically stable TGB$_A$ order between the N* and SmA phases. Note that the anomaly appearing on the high-temperature wing is the BPI–N* transition, shifted downwards as a result of the BP stabilization.[29]

The inset in Fig. 1 shows the dual feature of the lowest temperature C_p anomaly. This feature is indicative of a SmA–TGB$_A$ and a subsequent TGB$_A$–N$_L^*$ transition, where N$_L^*$ denotes a TGB$_A$ structure of shorter range order referred to as the chiral line liquid phase.[33] This double feature, together with a broad C_p anomaly related to the continuous conversion of the N$_L^*$ to N* phase, is a typical TGB$_A$ fingerprint.[25] This is additionally confirmed by SAXS measurements presented in Fig. 2. The temperature evolution of the full-width at half-maximum

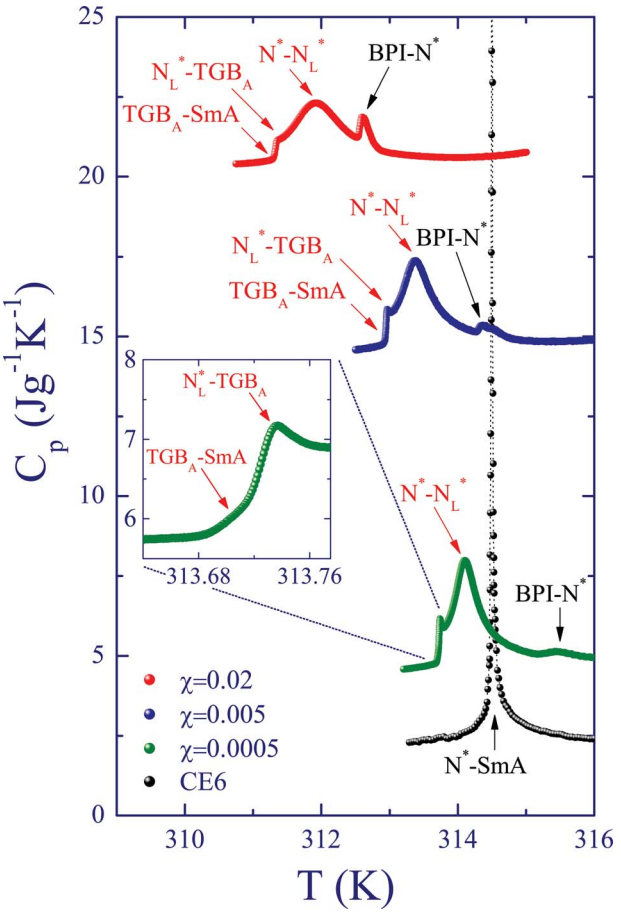

Fig. 1 The temperature profiles of C_p obtained by ASC upon cooling (rate of 1.6 mK min^{-1}) are shown for the pure CE6 and the mixtures with $\chi = 0.0005$, 0.005 and 0.02. CE6 exhibits a sharp, direct N*–SmA transition, while all mixtures exhibit an essentially wider double-peak anomaly, marking the presence of the TGB$_A$ order. The inset shows that the low-temperature anomaly also consists of a dual peak, identified as the unique pattern of a SmA–TGB$_A$–N$_L^*$ phase sequence.[25]

(FWHM) and the maximum scattered intensity (I_o) clearly support the presence of TGB$_A$ and N$_L^*$ phases. I_o and FWHM, plotted on the same temperature scale with C_p data for $\chi = 0.02$, demonstrate the gradual loss of the quasi-long-range smectic order along the N$_L^*$ phase, exactly as observed in the pioneering experiments on TGBs by Navailles *et al.*[34]

Additional evidence related to the presence of the TGB$_A$ order is provided by POM textures. Both homeotropic and planar anchoring conditions were imposed on the samples. Textures observed under POM for homeotropic cells are shown in Fig. 3(a). The images corresponding to pure CE6 are presented in the left-hand column. In the SmA phase (top row) the director is parallel to the direction of the light propagation resulting in dark images between crossed polarizers. A typical chiral nematic N* texture is also found at higher temperatures (bottom row). Of particular interest is the texture appearing in the coexistence region of the first-order N*–SmA transition. Here N* islands or stripes evolve and supersede the dark SmA phase on heating. However, a completely different texture is observed for the CE6 + CdSe $\chi = 0.02$ mixture (central column). Here very thin, bright and stable filaments emerge upon heating

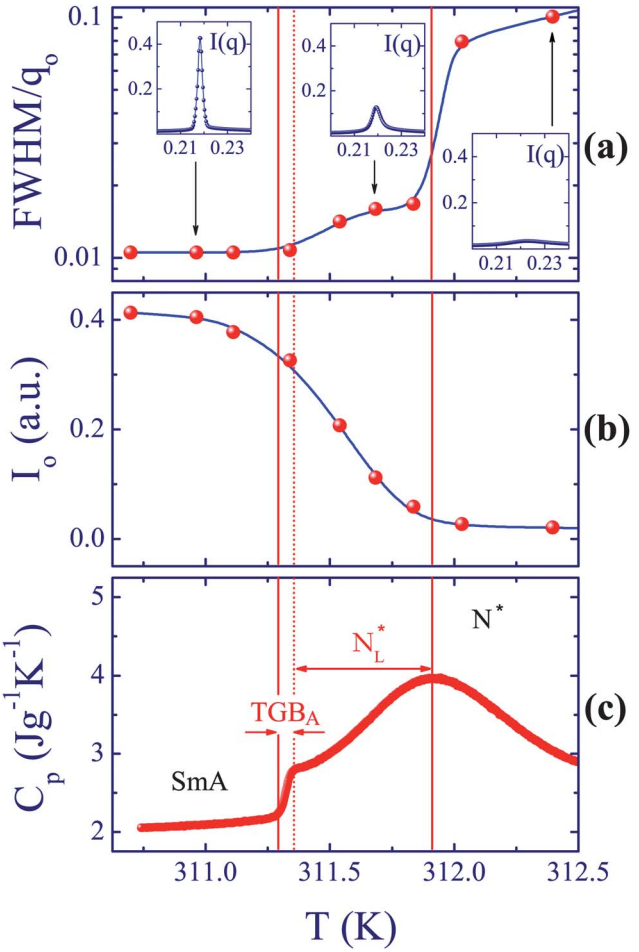

Fig. 2 The FWHM (a) and I_o profiles (b), obtained by SAXS, are shown on the same temperature scale with the C_p data (c) for the $\chi = 0.02$ sample. The FWHM evolution demonstrates the gradual loss of the quasi-long range order along the N_L^* phase range. The significant change of the scattered intensity along the different LC phases is visualized in the insets. Although FWHM changes only slightly along the region of the established TGB_A order, I_o decreases substantially, displaying the fingerprint of the N_L^* phase[34] between TGB_A and N^*. Note that q_o refers to the q value corresponding to the maximum intensity I_o.

from the dark SmA phase, growing into an immaculate filament network (middle row) characteristic of the TGB_A structure.[28]

Similar differences between the textures of pure CE6 and the mixture with $\chi = 0.02$ are observed in the planar cells, shown in Fig. 3(b). In the SmA phase of both CE6 (left column) and $\chi = 0.02$ mixture (central column), the characteristic focal conic texture is observed, exhibiting only a color difference due to the presence or absence of NPs. The textures in the N^* phase are also similar (bottom row). However, they are quite different at intermediate temperatures, corresponding to the N^*, SmA phase-coexistence region of CE6 (left) and the stable TGB_A structure of the $\chi = 0.02$ mixture (center). For the TGB_A phase different color regions evidence the continuous twist of the smectic slabs, resulting in a helical and birefringent structure perpendicular to the glass plates. From the POM images we conclude that in the $\chi = 0.02$ mixture a stable TGB_A structure is observed upon heating from SmA or cooling from the N^* phase.

Note that the textures specified as TGB_A in Fig. 3 are obtained on the edge between TGB_A and N_L^* phases for the $\chi = 0.02$ sample. No difference was observed in textures slightly above or below the specified temperature, *i.e.*, at temperatures belonging to TGB_A and N_L^* phases according to ASC data. Since both these phases exhibit exactly the same kind of order (being long-range for TGB_A and progressively changing to short-range for N_L^*), their distinction based on POM might be unattainable. Moreover, the imposed anchoring conditions (planar or homeotropic) in the sample–glass interfaces can additionally obstruct such a distinction.

Finally, the phase diagram of the system CE6 + NPs is depicted in Fig. 4. The inset shows the temperature window $\Delta T_{TGB_A+N_L^*}$ of the stable TGB_A order, *i.e.*, the joined range of TGB_A and N_L^* phases. The phase transition lines are drawn based on the ASC data that are the most reliable in terms of temperature precision.

V Mean-field estimates

In the following we estimate the impact of NPs on the TGB_A phase stability range using the phenomenological free energy expression introduced in Section III. We illustrate the impact of NPs on the temperature stability width $\Delta T_{TGB_A+N_L^*}(\chi) = T_N - T_{TGB\text{-}SmA}$ of LC structures dominated by screw dislocations. Here $T_{TGB\text{–}SmA}$ stands for the TGB_A–SmA phase transition and T_N estimates the temperature of the N^*–N_L^* phase transformation. The TGB_A structure is characterized by a well-defined, one-dimensional lattice of screw dislocations. On the contrary, in the N_L^* phase the dislocations strongly oscillate.[35] Within a mean-field-type approach the differences between the TGB_A and N_L^* structures are neglected and, henceforth, we use the former configuration as the representative defect structure.

The main characteristic geometric features needed for the derivation are shown in Fig. 5(a). The TGB_A phase consists of slabs of length l_b exhibiting essentially bulk SmA ordering. The slabs are separated by grain boundaries (GBs) of width given roughly by the nematic twist penetration length λ. Parallel screw dislocations reside within each GB, separated by a distance[23] $l_d \sim l_b$. Globally, the system exhibits a helical structure due to the tilt between the adjacent slabs, which is enabled by screw dislocations. The volume of a representative TGB_A unit cell, consisting of a SmA slab and a GB, is given by $V_u \sim l_b l^2$, where the grain boundary surface is set to be equal to l^2. The average dislocation length is approximated by l. Hence, the number N_{def} of defects within a GB is $N_{def} \sim l/l_d \sim l/l_b$.

A Free energy costs of competing phases

Here the free energy costs $\Delta F^{(phase)}$ related to the N^*, SmA and TGB_A order formation are estimated within a unit cell V_u.

The ordering within the N^* phase is described using the Cartesian frame (x, y, z) by $\eta_s = 0$, $\vec{n} = (\sin\theta, \cos\theta, 0)$ where $\theta = q_{ch}z$. The corresponding spatially averaged free energy density $f^{(phase)} = \Delta F^{(phase)}/V_u$ equals

$$f^{(N^*)} = 0. \quad (9)$$

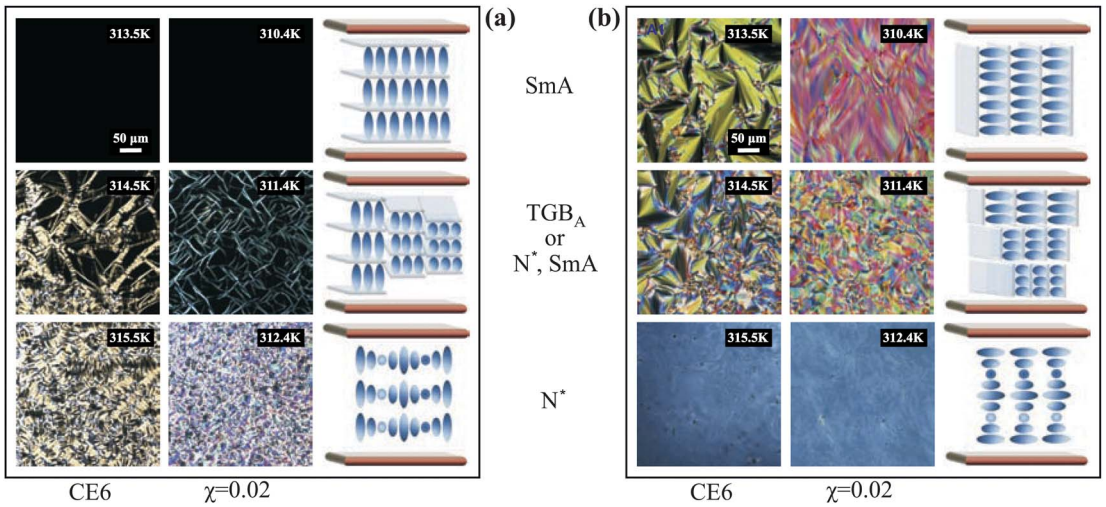

Fig. 3 (a) Homeotropic cells: textures of pure CE6 (left column) and $\chi = 0.02$ mixture (central column). The dark textures at the top correspond to SmA phase, while the images at the bottom to the N* phase. In the middle, mixed textures of coexisting N*, SmA domains are depicted for CE6, while a TGB$_A$ filament structure is revealed for $\chi = 0.02$. (b) Planar cells: textures of pure CE6 (left column) and $\chi = 0.02$ mixture (central column). The textures at the bottom and top correspond to N* and SmA phases, respectively. In the middle, mixed N*, SmA domains are observed for CE6 and a more colorful TGB$_A$ texture for $\chi = 0.02$, resulting from the continuous twist of the smectic slabs. A scheme of the ideal molecular orientation for each structure is depicted in the right-hand columns of both (a) and (b).

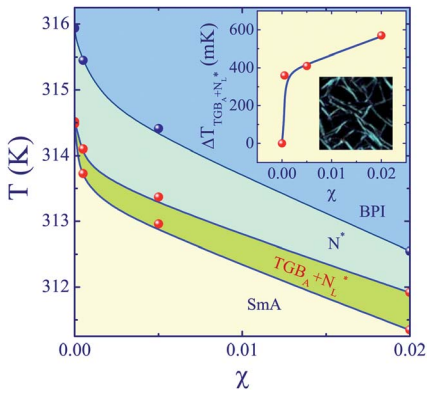

Fig. 4 The temperature *versus* concentration (T–χ) phase diagram of the system CE6 + NPs constructed from ASC, SAXS and POM measurements. The inset shows the range $\Delta T_{TGB_A+N_L^*}$ of the induced TGB$_A$ order as a function of χ. This order is of long-range (TGB$_A$) and it progressively changes to a shorter range (N$_L^*$) upon increasing T.

The SmA ordering within a unit cell can be determined by $\vec{n} = (1,0,0)$ and $\psi = \eta_s e^{iq0x}$. It follows

$$f^{(\mathrm{SmA})} = -\frac{\alpha_0|t|^2\eta_0{}^2}{2} + \frac{K_2 q_{\mathrm{ch}}{}^2}{2}. \quad (10)$$

To estimate the free energy costs for the formation of a TGB$_A$ structure it is assumed that within the smectic blocks an ideal SmA ordering is established and the structure exhibits on average a twist along the z-coordinate. The presence of the twist is enabled by the incorporation of screw line dislocations at GBs. Across each GB (the width of which is roughly given by λ) the director field is approximately rotated by an angle[23]

$$\Delta\theta \sim \frac{d}{l_{\mathrm{d}}} \sim \frac{d}{l_{\mathrm{b}}}. \quad (11)$$

Consequently, the orientational elastic penalties are given by

$$\int_0^{l_{\mathrm{b}}} \mathrm{d}z\left(\vec{n}\cdot(\nabla\times\vec{n}) - q_{\mathrm{ch}}\right)^2 \sim \frac{\Delta\theta^2}{\lambda} - 2q_{\mathrm{ch}}\Delta\theta + q_{\mathrm{ch}}{}^2 l_{\mathrm{b}}.$$

Within the cores of screw dislocations SmA ordering is essentially melted. The resulting average smectic condensation free energy within a volume V_{u} reads

$$F_{\mathrm{c}}^{(\mathrm{TGB})} = -\frac{\alpha_0|t|^2\eta_0{}^2}{2}\left(V_{\mathrm{u}} - V_{\mathrm{def}}\right), \quad (12)$$

where $V_{\mathrm{def}} \sim N_{\mathrm{def}} l\pi\xi^2 \sim l^2\pi\xi^2/l_{\mathrm{b}}$ is the volume occupied by the core defects. We further neglect other elastic contributions (*e.g.*, interactions among dislocations) that play a secondary role if $l_{\mathrm{b}} \gg \lambda$.

With this in mind we obtain

$$f^{(\mathrm{TGB})} = \frac{K_2}{2}\left(\frac{\Delta\theta^2}{\lambda l_{\mathrm{b}}} - \frac{2q_{\mathrm{ch}}\Delta\theta}{l_{\mathrm{b}}} + q_{\mathrm{ch}}{}^2\right) - \frac{\alpha_0|t|^2\eta_0{}^2}{2}\left(1 - \frac{\pi\xi^2}{l_{\mathrm{b}}{}^2}\right). \quad (13)$$

Next, the addition of NPs is considered with an average volume density

$$\phi = (N_{\mathrm{NP}} v_{\mathrm{NP}})/V_{\mathrm{u}} \sim \chi(\rho_{\mathrm{LC}}/\rho_{\mathrm{NPs}}).$$

Here N_{NP} stands for the number of NPs within V_{u}, v_{NP} is the average volume of one nanoparticle, and ρ_{NP} and ρ_{LC} stand for the mass densities of NPs and LC, respectively. It is assumed that the NPs are predominantly assembled at the dislocation cores. Furthermore, we assume that the main impact of NPs from the energy point of view is their effect on the condensation free energy penalty within the cores of defect.

Taking this into account, the condensation free energy $F_{\mathrm{c}}^{(\mathrm{TGB})}$ within V_{u} reads

$$F_{\mathrm{c}}^{(\mathrm{TGB})} = -\frac{\alpha_0|t|^2\eta_0{}^2}{2}\left(V_{\mathrm{u}} - V_{\mathrm{def}} + N_{\mathrm{NP}} v_{\mathrm{NP}}\right). \quad (14)$$

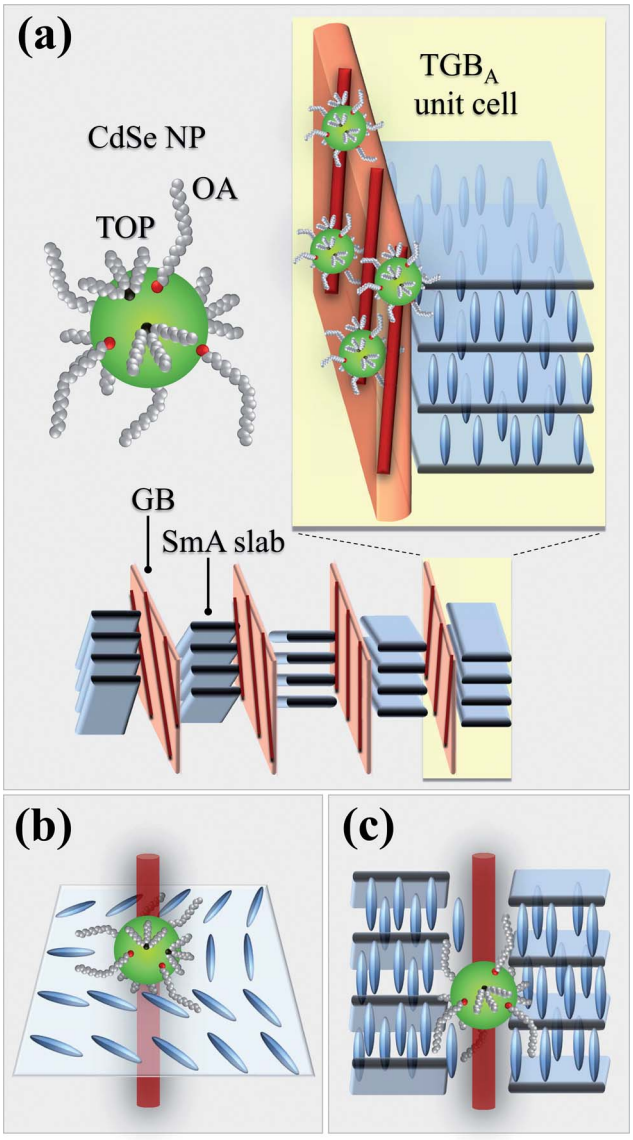

Fig. 5 (a) CdSe nanoparticles (top left), with a core diameter of 3.5 nm, surface-treated with OA and TOP, induce a TGB_A order by stabilizing the lattice of screw dislocations at GBs separating the twisting smectic slabs (bottom). A blow-up of the TGB_A unit cell is presented at the top right. (b and c) The adaptive character of CdSe NPs, enabled by their size and flexible surface chains, is depicted. The NPs accommodate with the average local orientational order of the qualitatively different nematic disclination lines (b) and smectic screw dislocations (c). Note that this figure serves as an illustrative picture without aiming to precisely represent the relative sizes of the components.

If the added NPs are adaptive with respect to the neighboring LC order they relatively weakly disturb the latter. In this case the additional elastic free energy costs due to NPs are negligible. Consequently, the overall impact of NPs is a decrease in the singular defect core volume free energy. If the NPs are not adaptive they could significantly distort locally the LC ordering. In order to estimate the consequent impact it is assumed that only the smectic degree of ordering is affected. This order is enforced to be melted at the surface of NPs. For simplicity we neglect the local distortions in the LC orientational ordering that would further enlarge the elastic costs. Hence, the additional smectic elastic penalty costs are given by

$$\Delta F_e^{(TGB)} \sim N_{NP} V_m \left| f_c^{(s)} \right| \sim \left| f_c^{(s)} \right| \phi \frac{\omega \pi l^2 l_d \xi}{r}, \qquad (15)$$

where V_m estimates the volume of the essentially melted region that surrounds an effectively spherical NP characterized by radius r and $\omega \sim 1$.

Therefore, if NPs are present, we obtain

$$f^{(TGB)}(\phi) \sim \frac{K_2}{2}\left(\frac{\Delta\theta^2}{\lambda l_b} - \frac{2q_{ch}\Delta\theta}{l_b} + {q_{ch}}^2\right) - \frac{\alpha_0 |t|^2 {\eta_0}^2}{2}\left(1 - \frac{\pi\xi^2}{{l_b}^2} + \phi\left(1 - \frac{\omega\pi\xi}{r}\right)\right). \qquad (16)$$

B Phase transition behavior

The phase behavior in the absence of NPs is first considered. If the chirality is not strong enough then on lowering temperature the N^* phase directly transforms into the SmA order without an intermediate TGB_A structure. The corresponding phase transition temperature T_{NA} is determined by the condition $f^{(SmA)} = f^{(N^*)}$. Using eqn (9) and eqn (10) it follows $r_{NA} = -\lambda_0 \xi_0 q_0 q_{ch}$, *i.e.*

$$T_{NA} = T_*(1 - \lambda_0 \xi_0 q_0 q_{ch}). \qquad (17)$$

If the chirality is strong enough then the TGB_A phase intervenes between N^* and SmA ordering. The N^*–TGB_A transition temperature T_N is determined by the condition $f^{(N^*)} = f^{(TGB)}$. Using eqn (9) and eqn (13) we obtain

$$T_N = T_*\left(1 - \lambda_0 \xi_0 q_0 q_{ch} \sqrt{\frac{1 + \frac{d^2}{\lambda {l_b}^3 {q_{ch}}^2} - \frac{2d}{q_{ch} {l_b}^2}}{1 - \pi\xi^2/{l_b}^2}}\right). \qquad (18)$$

The measurements suggest that the CE6 + NP system is close to a triple point, where the onset of TGB_A and SmA coincides on decreasing temperature from the N^* phase. The triple point is determined by the condition $T_N = T_{NA}$. The corresponding chirality strength $q_{ch}^{(t)}$ fulfills the equation

$$q_{ch}^{(t)} \sim \frac{d}{\pi\xi^2}\left(1 - \sqrt{1 - \frac{\pi\xi^2}{\lambda l_b}}\right). \qquad (19)$$

Therefore, in the limit $l_b \sim l_d \to \infty$ where SmA and TGB_A phases are almost indistinguishable, it follows $q_{ch}^{(t)} \sim 0$ as it should.

For $q_{ch} = q_{ch}^{(t)}$ the added NPs stabilize the TGB_A structure in a finite temperature interval providing they are adaptive, *i.e.* $\frac{\omega\pi\xi}{r} < 1$ (see eqn (16)). The TGB_A–SmA transition temperature $T_{TGB-SmA}$ is determined by the condition $f^{(TGB)} = f^{(SmA)}$. Therefore, in the adaptive regime $(\frac{\omega\pi\xi}{r} < 1)$ it holds

$$\Delta T_{TGB_A + N_L^*}(\chi) \sim (T_* - T_{NA})\,\frac{\phi}{2}\frac{{l_b}^2}{\pi\xi^2}\left(1 - \frac{\pi\omega\xi}{r}\right) \sim (T_* - T_{NA})\,\frac{\chi\rho_{LC}}{2\rho_{NPs}}\frac{{l_b}^2}{\pi\xi^2}\left(1 - \frac{\pi\omega\xi}{r}\right). \qquad (20)$$

VI Discussion

The present observations infer that surface-functionalized CdSe NPs efficiently stabilize networks of screw dislocations. In the following we discuss the conditions enabling the stabilization by using the estimates derived above. We claim that the key mechanism behind this is the defect-core replacement effect, as first discussed by Kikuchi *et al.*[13] According to it the condensation free energy penalty due to the presence of topological defects is substantially reduced if NPs replace a substantial part of their defect-core volume. This is illustrated in eqn (14) where NPs trapped within screw dislocations reduce the total volume where the smectic order is essentially melted due to topological reasons. However, this free energy gain could be wasted if NPs apparently disrupt the defect-core structure. Such additional penalties for specific "non-favorable" boundary conditions at NP–LC interfaces are estimated in eqn (15) where only the deformations in smectic ordering are considered. In our samples NPs can adapt to a defect core structure due to their size and attached flexible chains. One might argue that the NP-driven stabilization is most effective if NPs do not interact with LC and their impact is embodied only *via* the defect-core volume replacement effect. However, in this case the targeting of NPs towards topological defects would not be efficient and would be driven solely by Brownian motion. For this reason NPs should weakly interact with the smectic phase factor ϕ (see eqn (1)). It namely represents the gauge component of the smectic order parameter which possesses a Goldstone mode. Consequently, the coupling between NPs and ϕ enables the propagation of long-range interactions.[12,36,37] It has been shown that homogeneously dispersed NPs alter the average layer spacing.[37,38] Such configuration changes are relatively energetically costly and the resulting forces could be relatively large. Note that the phase transition temperature in the SmA phase apparently decreases on increasing χ (see Fig. 4) revealing elastic distortions in the gauge component of the order parameter.[36,37] We further note that if NPs are small enough to fit inside the cores of defects, their interactions with the gauge field are substantially reduced due to the essentially melted order parameter within the cores.

In Section V it has been shown that NPs could trigger the onset of TGB_A ordering although it is absent in a pure LC sample if the chirality is not strong enough. In our theoretical estimate the triple point conditions (eqn (19)) were considered, where all the competing (N^*, TGB_A, SmA) phases coexist for $\chi = 0$, as suggested by the experimental results. In the case of adaptive nanoparticles the TGB_A ordering is established for $\chi > 0$. In the diluted regime our estimate suggests $\Delta T_{TGB_A+N_L^*}(\chi) \propto \chi$ (see eqn (20)), which is in line with the experimental measurements (see inset of Fig. 4).

Furthermore, previous studies have revealed that the same NPs essentially stabilize disclination lines in BPs.[14,29,39] The core structures of nematic disclinations (see Fig. 5(b)) and smectic screw dislocations (see Fig. 5(c)) are qualitatively different. The CdSe NPs are efficiently trapped into both defects due to their size and attached flexible chains which enable their adaptability. Simulations have revealed that NPs tend to aggregate in regions exhibiting configurations compatible with the conditions at the NP–LC interface.[39]

To our knowledge, no other study has so far revealed such a phenomenon, *i.e.*, the simultaneous stabilization of disclination lines and screw dislocations by the same type of NPs. The efficient trapping of NPs within these qualitatively different networks of topological defects is enabled by a set of conditions referred to as the ADCT mechanism. One may argue that a critical (upper) size of NPs is expected for their adaptability to the cores of defects. Note that in our theoretical modeling it is assumed that the radius r of NPs is smaller than the defect core size which is roughly comparable to ξ. This scenario is realized in the case of CdSe nanoparticles. In the case of $r > \xi$ the NPs are expected to disrupt the phase of smectic ordering and, hence, the energy penalties gained by the defect-core-replacement would be reduced. The importance of the spherical NP size has been very recently reported in the case of BP stabilization,[40] where particles larger than 100 nm have been proven ineffective with respect to essentially smaller ones. Further experimental studies are needed to confirm the validity of such an assumption in the case of screw dislocations.

VII Conclusions

In summary, it is demonstrated that the ADCT mechanism efficiently stabilizes lattices of screw dislocations using surface-functionalized CdSe NPs. The same NPs also stabilize the qualitatively different line disclinations in BPs,[14] proving the robustness of ADCT. Note that CdSe NPs are typical quantum dot representatives exhibiting size-dependent photoluminescence.[10]

The ADCT mechanism could be exploited for diverse applications. It could be used to enhance the stability range of diverse periodic structures with potential use in display or photonic applications,[41] where the periodicity and the related desired optical properties arise due to defect lattices. In addition, the ADCT-driven trapping of appropriate NPs triggering nucleation and stabilization of structures possessing topological defects could be exploited for designing sensitive NP detectors, provided that the defect patterns are clearly visible by means of optical methods. The present as well as previous studies[14] reveal that even minute concentrations of NPs can substantially increase the stability of structures dominated by topological defects. A closely related mechanism has been recently demonstrated,[42] where ppm concentrations of endotoxin were sufficient to trigger a structural transition in a solution of micrometer-sized LC droplets. ADCT is also of great importance towards the controlled assembly of NPs in soft, anisotropic media. The trapped NPs are exploited as functionality-conveying agents, as it has been recently demonstrated in the case of photoluminescence of CdSe quantum dots,[10] the surface plasmon resonance of gold[4,43] and the multiferroic behavior of LC and γ-Fe_2O_3 nano-composites.[44]

The direct analogy between LC screw dislocations and magnetic vortices[20,45] infers that the understanding and mastering of the universal ADCT mechanism could contribute to resolving several enigmatic phenomena in magnetism.

Magnetic vortices exhibit a rich diversity of complex structures,[45] and the impact of disorder on their static and dynamic properties is far from being fully understood.[46] The easily accessible configurations of LCs + NPs may serve as an additional experimental testing ground to gain an insight towards the impurity-driven pinning of vortices in superconductors.[47]

Acknowledgements

This work has been supported by the Project PE3-1535 within the Action "Supporting Postdoctoral Researchers" of the Operational Program "Education and Lifelong Learning", co-financed by the European Social Fund and the Greek State. S. D. acknowledges the funding of Projects DST (SR/NM/NS-134/2010(G)) and CSIR (03(1207)/12/EMR-II). S. K. acknowledges the support of the Project P1-0099. Z. K. acknowledges the Project P1-0125 and the Centre of Excellence "NAMASTE". C. G. acknowledges the support of the FWO Research Project G.0492.10. S. K., G. C. and Z. K. acknowledge the financial support of the European Office of Aerospace Research and Development Grant FA8655-12-1-2068. G. N. and V. T. acknowledge the support of the J. S. Latsis Public Benefit Foundation.

References

1 P. Poulin, H. Stark, T. C. Lubensky and D. A. Wietz, *Science*, 1997, **275**, 1770.
2 D. Pires, J. B. Fleury and Y. Galerne, *Phys. Rev. Lett.*, 2007, **98**, 247801.
3 D. K. Yoon, M. C. Choi, Y. H. Kim, M. W. Kim, O. D. Lavrentovich and H. Jung, *Nat. Mater.*, 2007, **6**, 866.
4 Q. Liu, Y. Cui, D. Gardner, X. Li, S. He and I. I. Smalyukh, *Nano Lett.*, 2010, **10**, 1347.
5 U. Tkalec, M. Ravnik, S. Čopar, S. Žumer and I. Muševič, *Science*, 2011, **333**, 62.
6 E. R. Soule, J. Milette, L. Reven and A. D. Rey, *Soft Matter*, 2012, **8**, 2860.
7 R. Basu, C. Rosenblatt and R. Lemieux, *Liq. Cryst.*, 2012, **39**, 199.
8 F. H. Li, O. Buchnev, C. I. Cheon, A. Clushchenko, V. Reshetnyak, Y. Reznikov and T. J. Sluckin, *Phys. Rev. Lett.*, 2006, **97**, 147801.
9 R. Basu and G. S. Iannacchione, *Phys. Rev. E: Stat., Nonlinear, Soft Matter Phys.*, 2010, **81**, 051705.
10 B. Kinkead and T. Hegmann, *J. Mater. Chem.*, 2010, **20**, 448.
11 A. C. Balazs, T. Emrick and T. P. Russell, *Science*, 2006, **314**, 1107.
12 M. Kleman and O. D. Lavrentovich, *Soft Matter Physics*, Springer-Verlag, Berlin, 2002.
13 H. Kikuchi, M. Yokota, Y. Hisakado, H. Yang and T. Kajiyama, *Nat. Mater.*, 2002, **1**, 64.
14 E. Karatairi, B. Rožič, Z. Kutnjak, V. Tzitzios, G. Nounesis, G. Cordoyiannis, J. Thoen, C. Glorieux and S. Kralj, *Phys. Rev. E: Stat., Nonlinear, Soft Matter Phys.*, 2010, **81**, 041703.
15 I. Muševič, M. Škarabot, U. Tkalec, M. Ravnik and S. Žumer, *Science*, 2006, **313**, 954.
16 J. Lagerwall, G. Scalia, M. Haluska, U. Dettlaff-Weglikowska, S. Roth and F. Giesselmann, *Adv. Mater.*, 2007, **19**, 359.
17 R. Basu and G. S. Iannacchione, *Phys. Rev. E: Stat., Nonlinear, Soft Matter Phys.*, 2009, **80**, 010701(R).
18 J. Milette, S. Relaix, C. Lavigne, V. Toader, S. J. Cowling, I. M. Saez, R. B. Lennox, J. W. Goodby and L. Reven, *Soft Matter*, 2012, **8**, 6593.
19 P. G. de Gennes, *Solid State Commun.*, 1972, **10**, 753.
20 S. R. Renn and T. C. Lubensky, *Phys. Rev. A*, 1988, **38**, 2132.
21 J. Goodby, M. A. Waugh, S. M. Stein, E. Chin, R. Pindak and J. S. Patel, *Nature*, 1989, **337**, 449.
22 H. T. Nguyen, A. Bouchta, L. Navailles, P. Barois, N. Isaert, R. J. Twieg, A. Maaroufi and C. Destrade, *J. Phys. II*, 1992, **2**, 1889.
23 H. S. Kitzerow, in *Chirality in Liquid Crystals*, ed. H. S. Kitzerow and C. Bahr, Springer, New York, 2001, p. 186.
24 J. Fernsler, L. Hough, R. F. Shao, J. E. Maclennan, L. Navailles, M. Brunet, N. V. Madhusudana, O. Mondain-Morval, C. Boyer, J. Zasadzinski, J. A. Rego, D. M. Walba and N. A. Clark, *Proc. Natl. Acad. Sci. U. S. A.*, 2006, **102**, 14191.
25 T. Chan, C. W. Garland and H. T. Nguyen, *Phys. Rev. E: Stat. Phys., Plasmas, Fluids, Relat. Interdiscip. Top.*, 1995, **52**, 5000.
26 L. Navailles, P. Barois and H. T. Nguyen, *Phys. Rev. Lett.*, 1993, **71**, 545.
27 V. Domenici, C. A. Veracini, V. Novotná and R. Y. Dong, *ChemPhysChem*, 2008, **9**, 556.
28 I. Dierking and S. T. Lagerwall, *Liq. Cryst.*, 1999, **26**, 83.
29 G. Cordoyiannis, P. Losada-Pérez, C. S. P. Tripathi, B. Rožič, U. Tkalec, V. Tzitzios, E. Karatairi, G. Nounesis, Z. Kutnjak, I. Muševič, C. Glorieux, S. Kralj and J. Thoen, *Liq. Cryst.*, 2010, **37**, 1419.
30 J. Thoen, G. Cordoyiannis and C. Glorieux, *Liq. Cryst.*, 2009, **36**, 669.
31 H. Amenitsch, S. Bernstorff, M. Kriechbaum, D. Lombardo, H. Mio, M. Rappolt and P. J. Laggner, *J. Appl. Crystallogr.*, 1997, **30**, 872.
32 S. Kralj and T. J. Sluckin, *Phys. Rev. E: Stat. Phys., Plasmas, Fluids, Relat. Interdiscip. Top.*, 1993, **48**, 3244(R).
33 R. D. Kamien and T. C. Lubensky, *J. Phys. I*, 1993, **3**, 2131.
34 L. Navailles, B. Pansu, L. Gorre-Talini and H. T. Nguyen, *Phys. Rev. Lett.*, 1998, **81**, 4168.
35 D. R. Nelson and H. S. Seung, *Phys. Rev. B: Condens. Matter Mater. Phys.*, 1989, **39**, 79153.
36 S. Kralj, G. Cordoyiannis, A. Zidanšek, G. Lahajnar, H. Amenitsch, S. Žumer and Z. Kutnjak, *J. Chem. Phys.*, 2007, **127**, 154905.
37 Z. Kutnjak, S. Kralj and S. Žumer, *Phys. Rev. E: Stat., Nonlinear, Soft Matter Phys.*, 2002, **66**, 041702.
38 G. Cordoyiannis, S. Kralj, G. Nounesis, Z. Kutnjak and S. Žumer, *Phys. Rev. E: Stat., Nonlinear, Soft Matter Phys.*, 2007, **75**, 021702.
39 B. Rožič, V. Tzitzios, E. Karatairi, U. Tkalec, G. Nounesis, Z. Kutnjak, G. Cordoyiannis, R. Rosso, E. G. Virga, I. Muševič and S. Kralj, *Eur. Phys. J. E*, 2011, **34**, 17.

40 I. Dierking, W. Blenkhorn, E. Credland, W. Drake, R. Kociuruba, B. Kayser and T. Michael, *Soft Matter*, 2012, **8**, 4355.
41 W. Y. Cao, A. Muñoz, P. Palffy-Muhoray and B. Taheri, *Nat. Mater.*, 2002, **1**, 111.
42 I. H. Lin, D. S. Miller, P. J. Bertics, C. J. Murphy, J. J. de Pablo and N. L. Abbott, *Science*, 2011, **332**, 1297.
43 D. Coursault, J. Grand, B. Zappone, H. Ayeb, G. Levi, N. Félidj and E. Lacaze, *Adv. Mater.*, 2012, **24**, 1461.
44 B. Rožič, M. Jagodič, S. Gyergyek, M. Drofenik, S. Kralj, G. Cordoyiannis and Z. Kutnjak, *Mol. Cryst. Liq. Cryst.*, 2011, **545**, 99.
45 G. Blatter, M. V. Feigel'man, V. B. Geshkenbein, A. I. Larkin and V. M. Vinokur, *Rev. Mod. Phys.*, 1994, **66**, 1125.
46 T. Nattermann and S. Scheidl, *Adv. Phys.*, 2000, **49**, 607.
47 A. Snezhko, T. Prozorov and R. Prozorov, *Phys. Rev. B: Condens. Matter Mater. Phys.*, 2005, **71**, 024527.